RSC Advances

ROYAL SOCIETY
OF CHEMISTRY

PAPER

View Article Online
View Journal | View Issue

Check for updates

Cite this: *RSC Adv.*, 2025, **15**, 48762

Enhancing the energy density of phosphorus doped mesoporous carbon nitride using redox mediated gel-polymer electrolyte

Mustapha Balarabe Idris,* Bhekie B. Mamba and Fuku Xolile

Received 15th October 2025
Accepted 26th November 2025

DOI: 10.1039/d5ra07907a

rsc.li/rsc-advances

The practical application of supercapacitors is often limited by their low energy density, which stems from restricted voltage windows and insufficient redox reactions. Here, a symmetric supercapacitor device combining phosphorus-doped mesoporous graphitic carbon nitride (P-Mg-CN) electrodes with a redox-mediated gel polymer electrolyte (R-mgpe) is developed. In a three-electrode configuration, P-Mg-CN exhibited a specific capacitance of 134 F g^{-1} in 1 M H_2SO_4, which increased to 398 and 207 F g^{-1} in hydroquinone-based redox electrolytes, respectively, respectively, due to additional faradaic contributions from the I^-/I_3^- and hydroquinone/benzoquinone (HQ/BQ) redox couples. The device exhibits a broad voltage window of 1.4 V and achieves a high specific capacitance of 142 F g^{-1} at a current density of 2 A g^{-1}. It also delivers an energy density of 38.66 Wh kg^{-1} at a power density of 2.8 kW kg^{-1}. Furthermore, it retains 95.89% of its initial capacitance after 10 000 cycles. These results demonstrate that integrating redox-mediated gel electrolytes with heteroatom-doped carbon nitrides effectively increases the energy density of symmetric supercapacitors while maintaining long-term stability.

1 Introduction

The rapid expansion of the portable electronics and electric vehicles market, along with the need to integrate renewable energy sources into the grid, has accelerated the demand for efficient energy storage systems.[1–3] The basic requirements for the anticipated energy storage system include high energy and power densities, a long cycle life, and an excellent safety profile. Although rechargeable batteries, including lithium-ion and nickel–metal hydride batteries, exhibit high energy densities in the range of 200 to 300 Wh kg^{-1}, these systems are often limited by inferior power density and cycle stability.[4,5] Conversely, supercapacitors have received considerable attention, thanks to their fast charge/discharge capability, ultra-high cycling stability, and extended working temperature range, among other reasons.[6–8] However, their practical deployment is often limited by relatively low energy density, typically in the range of 5–20 Wh kg^{-1}.[9] This necessitates the development of rational strategies in both electrode material design and electrolyte engineering to achieve balanced device performance.[10,11] Among various electrolytes, aqueous electrolytes are considered promising candidates for supercapacitor applications owing to their excellent ionic conductivity, low cost and eco-friendliness. Nevertheless, the narrow working voltage windows, the possibility of leakage, and the low thermal stability are among the limitations of this class of electrolyte.[12] A gel polymer electrolyte (GPE) is a type of electrolyte which consists of a polymer matrix combined with a liquid electrolyte.[13,14] GPEs have emerged as a promising alternative to pristine liquid electrolytes, combining the mechanical flexibility of the polymer matrix with the excellent ionic conductivity of liquid electrolytes.[15] In recent years, the addition of small amounts of redox additives, serving as redox-active mediators, during the preparation of GPEs has been shown to improve the charge storage capability of the GPEs by introducing an additional faradaic charge storage mechanism.[16–18] Therefore, this strategy not only improves the specific capacitance but also extends the working voltage window, thereby improving the energy density of the device. For instance, Ahmad *et al.* reported the supercapacitive performance of GPE derived from pectin and potassium iodide (KI) as a redox additive.[17] The supercapacitor device was fabricated using hierarchical porous activated carbons (ACs) derived from melon waste, and developed redox additive GPEs delivered an energy of ~34 Wh kg^{-1} at a power density of ~232.5 W kg^{-1} and exhibited decent cycling stability over ~8000 cycles. A solid-state supercapacitor was assembled using poly(vinyl alcohol) (PVA)/(KOH)/hydroquinone (HQ) as redox-mediated GPE by Jinisha *et al.*, which delivered an energy density of 33.15 Wh kg^{-1} at a power density of 689.58 W kg^{-1}.[19] A novel GPE composed of PVA, sodium alginate, $K_3[Fe(CN)_6]$ and Na_2SO_4 was prepared by Yang *et al.*[18] A symmetrical supercapacitor fabricated using the prepared electrolyte and activated carbon electrodes demonstrated an energy density of 6.88 Wh kg^{-1} at a power density of ~58 W kg^{-1}. Hyeon *et al.* developed a dual-

---

Institute for Nanotechnology and Water Sustainability, College of Science, Engineering and Technology, University of South Africa, Florida Science Campus, 1710, South Africa. E-mail: idrisbm@unisa.ac.za

functional redox-based GPE using ethyl viologen dibromide, LiCl, and polyzwitterionic polymer. A quasi-solid-state based on the developed electrolyte delivered an energy density of 542 Wh kg^{-1} at a power density of 2.88 kW kg^{-1}.[20] A soy protein-based porous membrane was mixed with Li_2SO_4 and KI to form the redox mediator GPE by Xun *et al.*, and a supercapacitor based on SPI-Li_2SO_4-100 wt% KI exhibited an energy density of 16.02 Wh kg^{-1} at a power density of 573.78 W kg^{-1}.[21]

Graphitic carbon nitride (g-CN) as a semiconducting and metal-free material has attracted significant attention owing to its high nitrogen content, layered architecture, excellent mechanical strength, decent chemical and thermal stability.[22,23] Besides, precursors for the synthesis of g-CN are readily available at low cost, making it a promising candidate for various energy storage and conversion applications.[24,25] In general, g-CN is prepared by facile direct thermal polycondensation of various nitrogen-rich precursors, including melamine, cyanamide, urea, *etc.*[26] Nonetheless, g-CN prepared by the above approach is non-porous with an inherent low specific surface area and thus exhibits low performance in applications where surface area plays an essential role, such as adsorption, catalysis, electrochemical energy storage and conversion, *etc.*[27–29] Furthermore, owing to the restricted movement of ions and electrons in bulk g-CN, it displays inferior ionic and electrical conductivities, thereby resulting in deteriorated rate performance when utilised for energy storage applications.[1] These challenges necessitated the adoption of various strategies, such as composite formation, textural and morphological engineering, surface functionalisation, doping, *etc.*[29,30,30–33] For instance, Huang *et al.*, reported the utilization of heterostructured $Ti_3C_2T_x$/g-CN as an electrode for solid-state supercapacitors, which delivered a specific capacitance of 414 F g^{-1} at a current density of 1 A g^{-1}.[34] Chaluvachar *et al.*, prepared a composite of g-CN with carbon quantum dot poly(3,4-ethylene dioxythiophene) through the electrodeposition technique, which exhibited a specific capacitance of 109.5 F g^{-1} at a current density of 0.2 A g^{-1}.[35] Of special interest, heteroatom doping can significantly enhance the electrochemical activity of g-CN by electronic conductivity modulation and introduction of surface defect sites.[36–38] Notably, phosphorus doping has been shown to effectively alter the electronic configuration of g-CN, which in turn creates new active sites for charge storage and improves electrolyte wettability.[39] Indeed, our group has investigated the effect of phosphorus doping on the capacitance properties of mesoporous g-CN (Mg-CN).[40] The study demonstrated that not only the amount of the phosphorus doping, but also the type of the phosphorus functionalities, such as P–O and C–P, dictate the overall capacitance properties of Mg-CN. Despite advances in both g-CN and phosphorus-doped (P-Mg-CN) materials, the energy density of P-doped MGCN-based supercapacitors remains limited. This limitation could be attributed to the constraints imposed by the purely double-layer nature and the limited surface pseudocapacitive contributions from the electrode material. This suggests that there are opportunities to enhance its energy density. In this work, we report a P-Mg-CN electrode material coupled with R-mgpe to achieve enhanced energy storage performance. The device exhibits a broad voltage window of 1.4 V and achieves a high specific capacitance of 142 F g^{-1} at 2 A g^{-1}, delivering an energy density of 38.66 Wh kg^{-1} at a power density of 2.8 kW kg^{-1}. Furthermore, it retains 95.89% of its initial capacitance after 10 000 cycles.

2 Experimental

2.1 Materials and methods

All chemicals used in this study were of analytical grade and were used as received from Sigma-Aldrich.

2.2 Synthesis of P-Mg-CN

P-Mg-CN is synthesised using the previously reported method with little modifications.[40] Typically, 0.3075 g of the sodium salt of carboxymethyl cellulose was dispersed into 20 mL of ethanol, followed by the addition of 40 mL of deionised water while stirring was maintained. To this homogenous solution, 4 g of hexamethylenetetramine and 0.5 mL of phosphoric acid were added, and the mixture was stirred for 20 minutes at 80 °C. Afterwards, the mixture was transferred to a Petri dish and dried overnight at 80 °C. The obtained product was ground into a fine powder and carbonised at 600 °C for 4 hours. The final black coloured product was washed with 1 M HCl, rinsed with deionised water and dried at 80 °C overnight (Scheme 1).

2.3 Synthesis of redox-mediated gel-polymer electrolyte

Typically, 1 g of PVA with an average molecular weight of 146 000–186 000 was added to 10 mL of deionised water under vigorous conditions at 95 °C for 2 h, followed by the addition of 10 mL of 1 M H_2SO_4. Afterwards, 10 mL of 0.05 M KI was added, and stirring was maintained for another 1 hour. The obtained gel was transferred into a Petri dish and frozen at −16 °C for 12 hours, then thawed at room temperature for 12 hours and labelled as H_2SO_4 + PVA + KI (Scheme 2).

2.4 Physiochemical characterisation

The Powdered X-Ray Diffraction (PXRD) pattern of P-Mg-CN was analysed using a Rigaku Smart Lab X-ray diffractometer, whereas the chemical composition in the P-Mg-CN sample was evaluated using a 400 series Spotlight PerkinElmer Fourier transform infrared (FTIR) spectrophotometer and X-ray photoelectron spectroscopy (Thermo ESCA lab 250Xi, equipped with Monochromatic Al ka). The surface morphology and microstructures in P-Mg-CN were studied using FEI Tennai F30-S TWIN high-resolution transmission electron microscope (HR-TEM) and ZEISS field-emission scanning electron microscope (FE-SEM). The thermal stability of analysis of both PVA and PVA + KI (R-mgpe) was assessed by recording thermogravimetry analysis using METTLER TGA 2 LF/1100/1283 from 25 to 900 °C under a nitrogen flow rate of 10 mL min^{-1}. The chemical bonding environment in both PVA and R-mgpe was evaluated using a 400 series Spotlight PerkinElmer FTIR spectrophotometer under ATR mode.

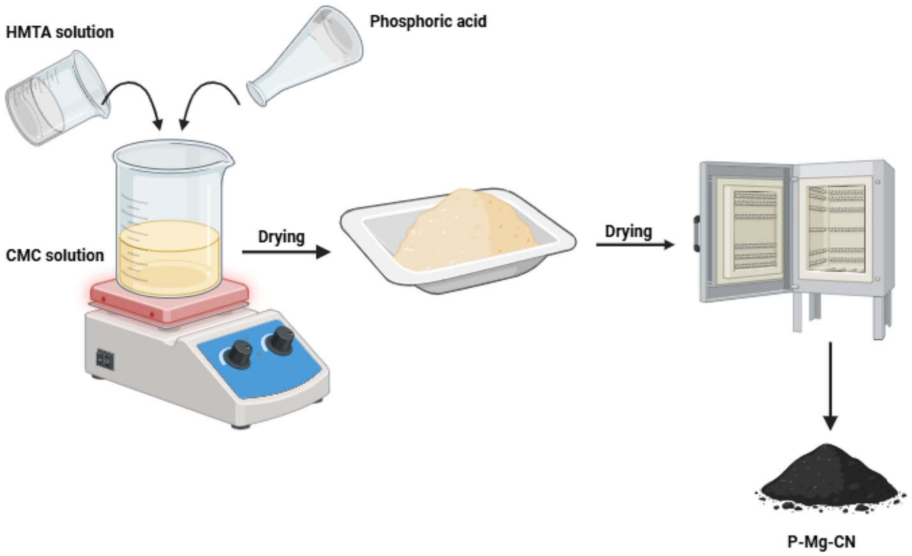

Scheme 1 Preparation of phosphoric doped mesoporous carbon nitride (P-Mg-CN).

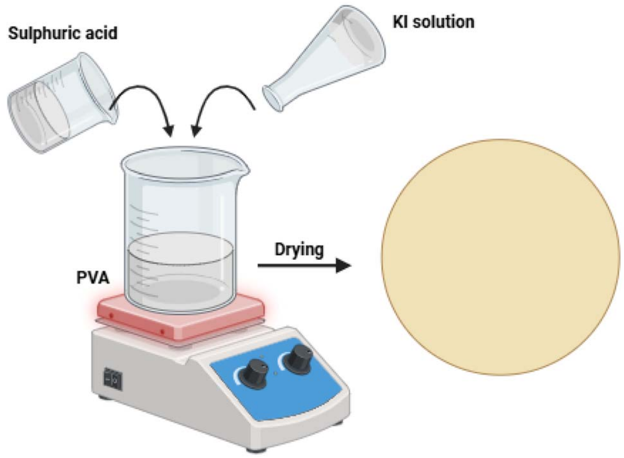

Scheme 2 Preparation of redox-mediated gel-polymer electrolyte (R-mgpe).

2.5 Electrochemical characterisation of P-Mg-CN electrode under three-electrode configuration

The capacitance properties of P-Mg-CN were firstly evaluated under a three-electrode system using Pt foil and Ag/AgCl as counter and reference electrodes, respectively. The P-Mg-CN working electrode was fabricated by mixing 80% of the active material, 10% of Super P carbon black and 10% of polyvinylidene difluoride binder. After the above mixture was manually ground, a few drops of *N*-methylpyrrolidone solvent were added to form a slurry, which was then coated onto a pretreated stainless steel foil and finally dried overnight at 80 °C. The capacitance properties of P-Mg-CN were recorded in both pristine (1 H_2SO_4) and redox-additive electrolytes (1 M H_2SO_4 + 0.05 M KI and 1 M H_2SO_4 + 0.05 M HQ) using a BioLogic VMP-3e Multichannel Potentiostat. The specific capacitance is calculated by integrating the area under the CV curve of the electrode using eqn (1).[15]

$$\text{Specific capacitance} = \frac{\int I\mathrm{d}v}{v \times \Delta V \times m} \tag{1}$$

where *I* is the current, *v* is the scan rate, *m* refers to the mass loading, and *V* is the potential window.

2.6 Fabrication and evaluation of a symmetrical supercapacitor

The working electrodes were prepared by casting a homogeneous slurry of P-Mg-CN onto one side of pretreated stainless steel foil current collectors with dimensions of 4 × 4 cm. The mass loading of the electrode material is maintained at 3.6 mg, equivalent to 0.225 mg cm^{-2}. Afterwards, the coated electrodes were dried at 80 °C and then assembled using a face-to-face configuration, with either H_2SO_4 + PVA or H_2SO_4 + PVA + KI gel serving as both separator and electrolyte. The sandwiched electrode and gel were wrapped using parafilm tape (Scheme 3). For comparison, a symmetrical supercapacitor is fabricated with pristine Mg-CN electrodes and R-mgpe as the electrolyte. The electrochemical performance of the fabricated devices was evaluated systematically using cyclic voltammetry (CV), galvanostatic charge–discharge (GCD), and electrochemical impedance spectroscopy (EIS). The specific capacitance (C, F g^{-1}), energy density (E, Wh kg^{-1}) and power density (P, W kg^{-1}) of the device were calculated using eqn (2)–(4), respectively.[41]

$$C = 2\frac{I\mathrm{d}t}{m\Delta V} \tag{2}$$

$$E = \frac{CV^2}{2} \times \frac{1000}{3600} \tag{3}$$

$$P = \frac{E}{t} \times 3600 \tag{4}$$

where *I* is the current in A, *m* is the mass of the material in the single electrode, Δ*V* is the voltage window of the device, *C* is the

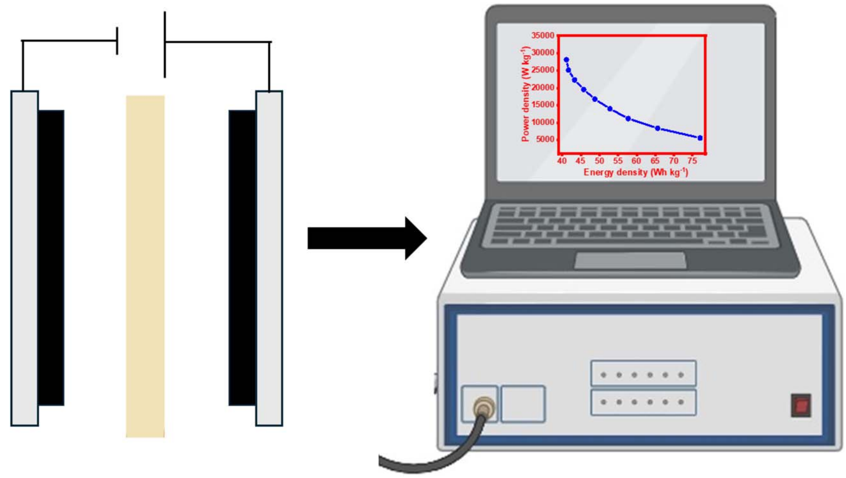

Scheme 3 Fabrication and testing of a symmetric supercapacitor device.

specific capacitance, V is the voltage, E is the energy density, P is the power density, and t is the discharge time.

The cycling stability of the P-Mg-CN device is assessed by subjecting it to 10 000 charge/discharge cycles at a current density of 7 A g^{-1}, followed by disassembly of the device. Subsequently, the electroactive material was carefully scraped from the SS foil and subjected to SEM analysis, whereas the R-mgpe gel was analysed by *ex situ* FTIR spectroscopy.

3 Results and discussion

3.1 Physicochemical characterisation of P-Mg-CN

The chemical structure and bonding environment of the P-Mg-CN is investigated using FT-IR spectroscopy and X-ray photoelectron spectroscopy (XPS). As seen in the FT-IR spectrum presented in Fig. 1a, the broad peak centred around 3435 cm^{-1} is assigned to the stretching vibrations of terminal amines and/

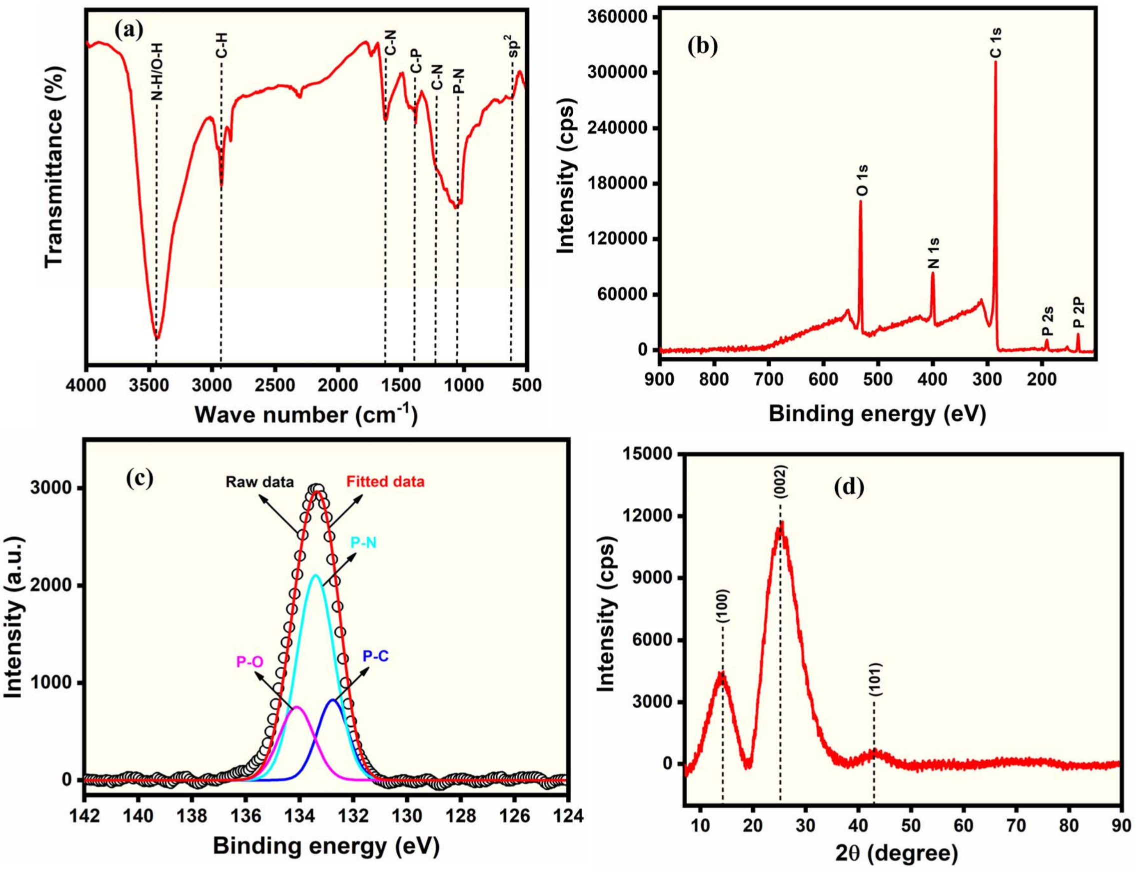

Fig. 1 (a) FT-IR, (b) XPS survey, (c) deconvoluted P 2p, core level spectra and (d) powered X-ray diffraction pattern of P-Mg-CN.

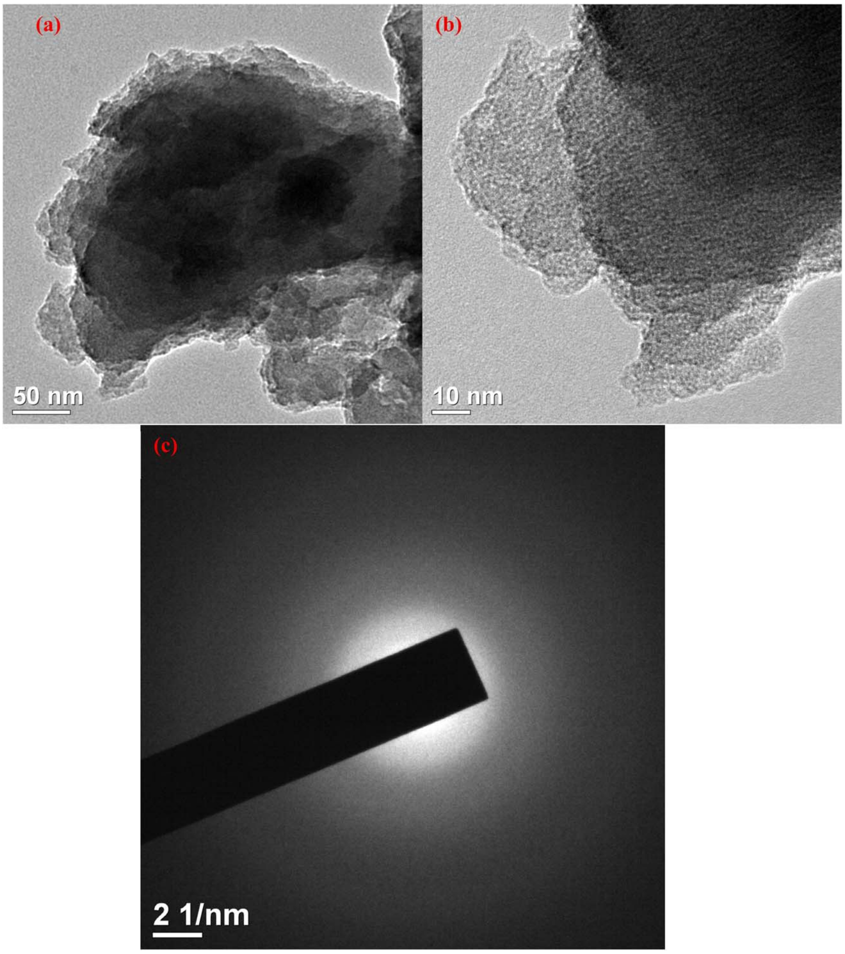

Fig. 2 (a and b) High-resolution TEM images, and (c) SAED image of P-Mg-CN.

or hydroxyl moieties.[39] While the peaks at 1630, 1232 and 1227 cm^{-1} are assigned to C═N stretching, the peaks at bands at 1380 and 1051 cm^{-1} are attributed to the characteristic of C–P and P–N bonds, respectively.[42] The hump-like peak at around 807 cm^{-1} corresponds to the tri-*s*-triazine units.[33,43] The low intensity of this peak suggests a slight distortion in the framework of g-CN after phosphorus incorporation. The shoulder-like peak witnessed at around 610 cm^{-1} is assigned to sp^2 domains found in amorphous carbon.[33,40] The XPS survey spectrum shown in Fig. 1b reveals the presence of carbon (C 1s), nitrogen (N 1s), oxygen (O 1s), and phosphorus (P 2p).[30] While C and N arise from the elemental building block of g-CN, O and P peaks indicate the successful doping of phosphorus (relative atomic weight of 5.79%) and partial surface oxidation, respectively.[44] To investigate the type of P doped into the frameworks of Mg-CN, the high-resolution P 2p spectrum is deconvoluted (Fig. 1c). The peaks centred at around 134.10, 133.40, and 132.60 eV are assigned to P–O, P–N and P–C, respectively.[45,46] The presence of P–N and P–C bonds indicates that phosphorus atoms are incorporated into g-CN frameworks by replacing nitrogen sites (P–N) and forming P–C bonds, respectively. On the other hand, the P–O bond suggests surface oxidation leads to P–O linkages. Fig. 1d presents the powder XRD (PXRD) patterns of P-Mg-CN. The diffraction peaks witnessed at $2\theta \sim 13.907$ and 25.36° correspond to the (100) and (002) planes in g-CN.[23] A slight reduction in the (002) peak intensity and a marginal shift toward a lower diffraction angle compared to the previously reported values for pristine g-CN indicate partial lattice distortion and expanded interlayer spacing caused by phosphorus incorporation.[47,48] The low intensity peak witnessed at around 43.28° corresponds to the (101) plane, which further suggests the presence of amorphous carbon.[49,50]

The morphological and microstructural features in P-Mg-CN were investigated by high-resolution TEM and FE-SEM, and the results are presented in Fig. 2. The TEM images shown in Fig. 2a and b, reveal the presence of a loosely stacked nanosheet-like morphology with abundant mesopores. The absence of well-defined lattice fringes in the high-resolution TEM image of P-Mg-CN confirms the amorphous nature of the sample and is consistent with the PXRD result. The selected area electron diffraction (SAED) image presented in Fig. 2c shows two diffuse concentric rings with no discrete reflections, a characteristic feature of partially amorphous g-CN domains, which is consistent with the PXRD results.

The SEM micrographs presented in Fig. 3a and b show that the P-Mg-CN electrode consists of loosely aggregated flakes and

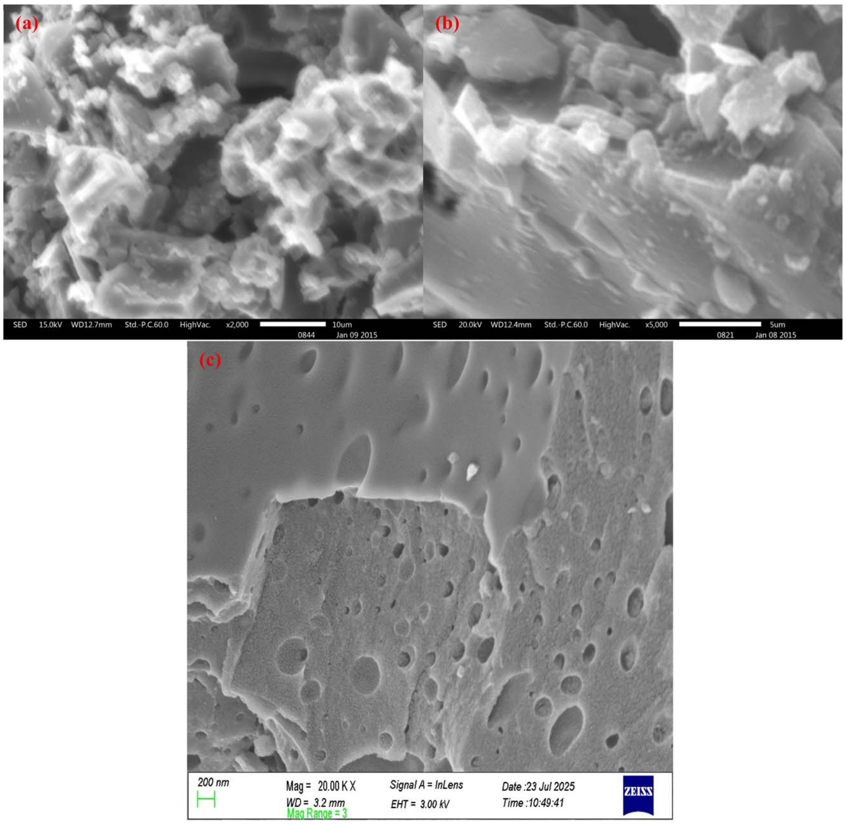

Fig. 3 (a–c) SEM images of P-Mg-CN recorded at various magnifications.

interparticle voids, which indicate the presence of mesopores. This architecture is expected to facilitate rapid ion diffusion and providing abundant electroactive sites for the I^-/I_3^--mediated pseudocapacitive processes occurring in the redox gel electrolyte. The high-magnification FE-SEM image (Fig. 3c) reveals an interconnected porous surface.

Fig. S1a shows the FTIR spectra of pristine PVA and KI-incorporated PVA (PVA + KI). The broad peak observed around 3390 cm^{-1} in the FTIR spectrum of PVA is assigned to O–H stretching vibrations arising from extensive inter- and intramolecular hydrogen bonding within the PVA framework.[51] Upon the incorporation of KI, a noticeable reduction in the O–H peak intensity and a marginal shift toward lower wavenumbers are observed in the FTIR spectrum of PVA + KI, which suggests that hydrogen-bond disruption caused by the dative bond interaction between K^+ ions and the hydroxyl groups.[52] The peaks observed in the FTIR spectra of both PVA and PVA + KI at around 2930 and 1430 cm^{-1} are assigned to C–H stretching and CH_2 bending, respectively. The peaks at around 1080 and 1140 cm^{-1} are assigned to C–O–C and C–O stretching vibrations, respectively. The intensities of these peaks decrease slightly and broaden in the KI-containing gel, attributed to coordination between the PVA chains and iodide species.[52] The thermograms of both PVA and PVA + KI are shown in Fig. S1b and exhibit the characteristic two-step degradation pattern. The initial mass loss below 150 °C corresponds to the removal of adsorbed water and loosely bound hydroxyl groups.[52] It can be observed that the PVA + KI shows slightly lower mass loss in this region, suggesting decreased water retention within the polymer network. The second weight loss observed in the thermograms of both samples, beyond 200 °C, is due to the thermal decomposition of the PVA matrix. The PVA + KI shows slightly lower mass loss in this region, indicating that KI enhances the thermal stability of the PVA frameworks.

3.2 Electrochemical characterisation of P-Mg-CN electrode under three configurations in pristine and redox additive electrolytes

The electrochemical performance of P-Mg-CN electrode is investigated under three electrolyte configurations using both pristine and redox additive electrolytes. Fig. 4a shows the cyclic voltammograms (CVs) recorded at a scan rate of 10 mV s^{-1} of P-Mg-CN electrode in both pristine and redox additive electrolytes. The CV profile of P-Mg-CN electrode in pristine electrolyte exhibits a nearly rectangular shape with humps-like features, an indication of charge storage by both mechanisms, namely, electrostatic adsorption/desorption at the electrode/electrolyte interfaces and surface faradaic contributions.[53,54] In contrast, the CVs of both H_2SO_4 + KI and H_2SO_4 + HQ present a broad profile with pronounced redox peaks. The I^-/I_3^- and HQ/BQ redox couples are responsible for the observed increases in the area under the CV and presence of well-defined redox peaks in the CV profile of P-Mg-CN in redox additive electrolytes. Indeed, the significantly enlarged integrated area of the KI and HQ-based

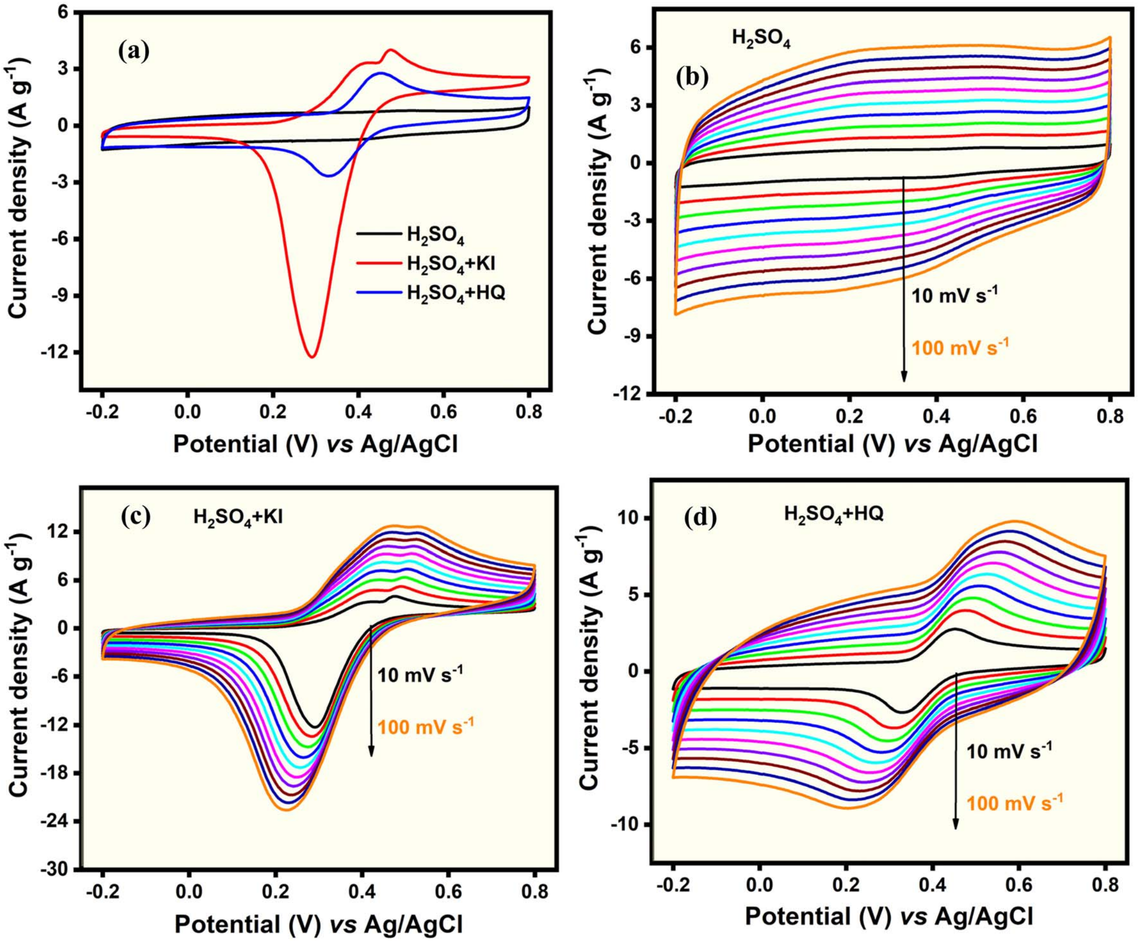

Fig. 4 (a) CV of P-Mg-CN recorded at a scan rate of 10 mV s^{-1} in M H_2SO_4, KI and HQ-based electrolytes. CVs of P-Mg-CN recorded at various scan rates in H_2SO_4 (b), H_2SO_4 + KI (c), and H_2SO_4 + HQ electrolyte (d).

electrolytes suggests enhanced charge-storage capability arising from electrostatic adsorption/desorption at the electrode/electrolyte interfaces and faradaic reactions of redox couples.[55] Furthermore, the higher current response observed in the KI-electrolyte as compared to the HQ system can be rationalised by ionic transport and interfacial kinetics. Iodide ions, being smaller, are expected to exhibit a faster diffusion rate and electron-transfer kinetics, leading to a higher current response. Fig. 4b–d show the CV curves recorded at various scan rates, ranging from 10 to 100 mV s^{-1}, in both pristine and redox-additive electrolytes. As shown in Fig. 4b–d, the CV curves of the P-Mg-CN electrode exhibit an increase in current with increasing scan rate in all the electrolytes, suggesting good electrochemical reversibility. It can be inferred that the CV curves of the P-Mg-CN electrode in the pristine electrolyte retain their shape even at higher scan rates, an indication that charges are predominantly stored through the adsorption/desorption of electrolyte ions at the electrode/electrolyte interface. On the other hand, the CV curves of P-Mg-CN in redox additives electrolyte deviate significantly from the quasi-rectangular shape (Fig. 4c and d), which is ascribed to the inherent sluggish reaction kinetics of redox couple transformation.[56,57] It is worth noting that the CV of P-Mg-CN in the H_2SO_4 + KI electrolyte exhibits two distinct anodic oxidation peaks but only a single cathodic reduction peak. The multi-step electrochemical process of iodide oxidation could be responsible for the observed asymmetric feature.[58–60] The oxidation of iodide in acidic media proceeds with the formation of molecular iodine, followed by a rapid chemical equilibrium that forms polyiodide species.[61] Considering that these species have different formation kinetics and formal potentials, it's plausible to speculate that the first anodic peak at a lower potential corresponds to the diffusion-controlled oxidation of free iodide to polyiodide, whereas the second, higher-potential anodic peak is attributed to the oxidation of surface-adsorbed or confined iodide/polyiodide species. On the other hand, the rapid equilibration and subsequent reduction of the formed oxidised species result in a single merged cathodic peak. While the enhanced charge storage capability of P-Mg-CN in HQ is attributed to proton-coupled electron transfer at the electrode/electrolyte interface (eqn (5)), reversible electron shuttling is responsible for enhancing the charge storage in the KI-based electrolyte (eqn (6)).

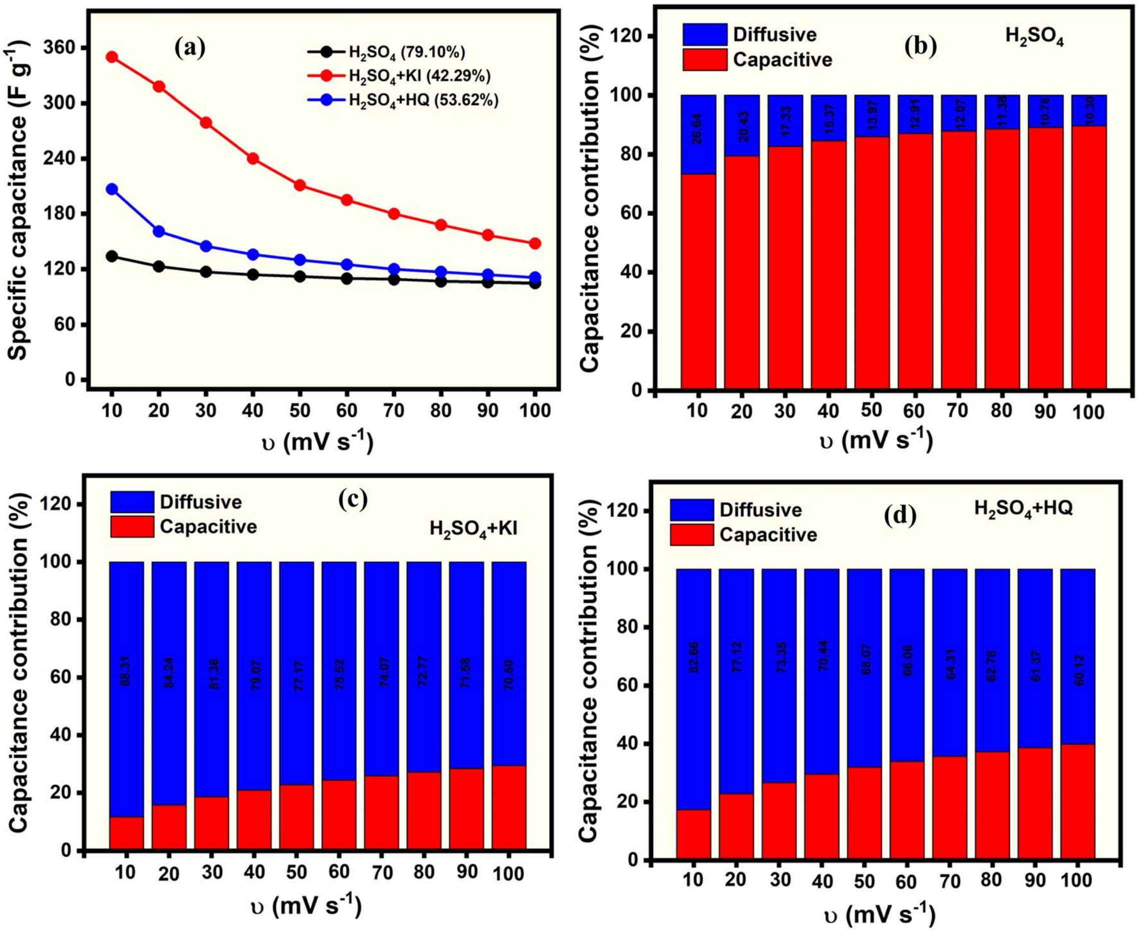

Fig. 5 (a) Rate performance of P-Mg-CN in both pristine and redox additive electrolytes. Percentage capacitance contribution in 1 M H_2SO_4 (b), H_2SO_4 + KI (c), and H_2SO_4 + HQ electrolyte (d).

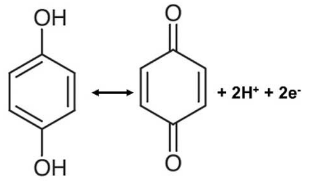

(5)

$$3I^- \leftrightarrow I_3^- + 2e^- \tag{6}$$

To quantitatively determine the value of the specific capacitance and variation of specific capacitance with scan rate of P-Mg-CN in both pristine and redox additive electrolyte, the CV curves were integrated and the results are presented in Fig. 5a. While P-Mg-CN electrode delivers a specific capacitance of 134 F g^{-1} at scan rate of 10 mV s^{-1} in pristine electrolyte, a specific capacitance of 398 and 207 F g^{-1} were obtained in KI and HQ based electrolyte respectively, at the same scan rates. This enhancement can be attributed to the additional faradaic reactions of I^-/I_3^- and HQ/BQ species. Although redox-based electrolytes exhibit higher specific capacitance at low scan rates, a significant decline in capacitance is observed with increasing scan rate, which is attributed to the decrease in capacitance contribution from the faradaic reaction at higher scan rates. To further investigate the charge-storage mechanism and separate the capacitive and diffusive contributions from the overall capacitance, Dunn's power-law relationship is employed.[62]

$$i(v) = k_1 v + k_2 v^{1/2} \tag{7}$$

$$\frac{i(v)}{v^{1/2}} = k_1 v^{1/2} + k_2 \tag{8}$$

where v and i denote the scan rate (mV s^{-1}) and current density (mA g^{-1}), k_1 and k_2 are the slope and intercept of the linear fit of $\frac{i(v)}{v^{1/2}}$ *vs.* $v^{1/2}$, respectively. After determining the slope and intercept, the percentage capacitive and diffusive contributions are calculated using eqn (9) and (10).

$$\text{Percentage capacitive contribution} = \frac{k_1 v}{k_1 v + k_2 v^{1/2}} \times 100\% \tag{9}$$

$$\text{Percentage diffusive contribution} = 100 - \text{capacitive contribution} \tag{10}$$

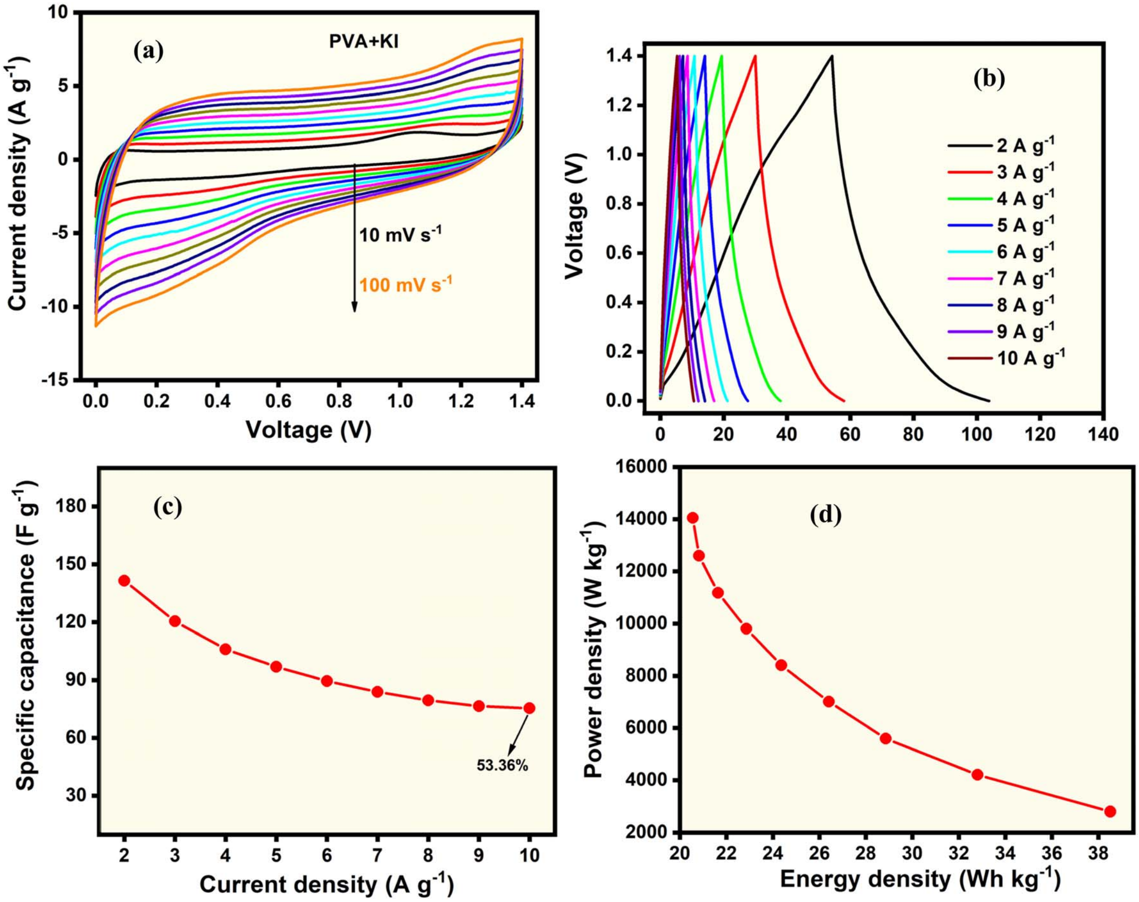

Fig. 6 (a) CVs of symmetrical device recorded at various scan rates in the range of 10 to 100 mV s^{-1}, (b) GCD curves recorded at various current densities in the range of 2 to 10 A g^{-1}, (c) rate performance and (d) Ragone plot of symmetrical devices in R-mgpe.

As shown in Fig. 5b, for P-Mg-CN in an H_2SO_4 electrolyte, the capacitive charge storage mechanism contributes to 73.36% at a scan rate of 10 mV s,[1] which increases to 89.70% when the scan rate is increased to 100 mV s^{-1}, indicating a surface-controlled process as the predominant charge storage mechanism. In contrast, both KI and HQ-based electrolytes demonstrate 88.31 and 82.66% of diffusive contribution at a scan rate of 10 mV s,[1] respectively, suggesting that the charge storage is governed by a diffusion-controlled process.

3.3 Electrochemical characterisation of a symmetrical supercapacitor in R-mgpe

A symmetric supercapacitor device was fabricated using the P-Mg-CN electrode and R-mgpe as both the separator and electrolyte. For comparison, a symmetrical supercapacitor is fabricated with pristine Mg-CN electrodes and R-mgpe as the electrolyte and results are presented in Fig. S2. While the use of PVA is expected to extend the working voltage of the device, the inclusion of KI in the gel electrolyte aims to introduce reversible redox reactions that can further enhance the pseudocapacitive contribution and overall energy density of the device. Fig. 6a presents the CV profiles recorded at scan rates ranging from 10

Table 1 Comparative energy and power density obtained in the present study with other carbonaceous materials in the redox additive electrolyte

Material	Electrolyte	Energy density (Wh kg^{-1})	Power density (W kg^{-1})	Reference
P-Mg-CN	PVA + H_2SO_4 + KI	38.66	2800	Present study
Date stone-derived activated carbon (AC)	PVA–H_2SO_4–anthraquinone	17.50	250	72
Active carbon cloth	Chitason-based hydrogels + Na_2MoO_4	34	1800	73
Reduced graphene oxide	K_2SO_4 + $K_3Fe(CN)_6$	36.8	1200	74
S-Doped graphene	H_2SO_4 + hydroquinone	27.00	810	74
Porous AC	Pectin-based polymer + LiCl + KI	34	232.5	17
AC	PVA–Li_2SO_4 + 1-butyl-3-methylimidazolium iodide	29.3	—	75

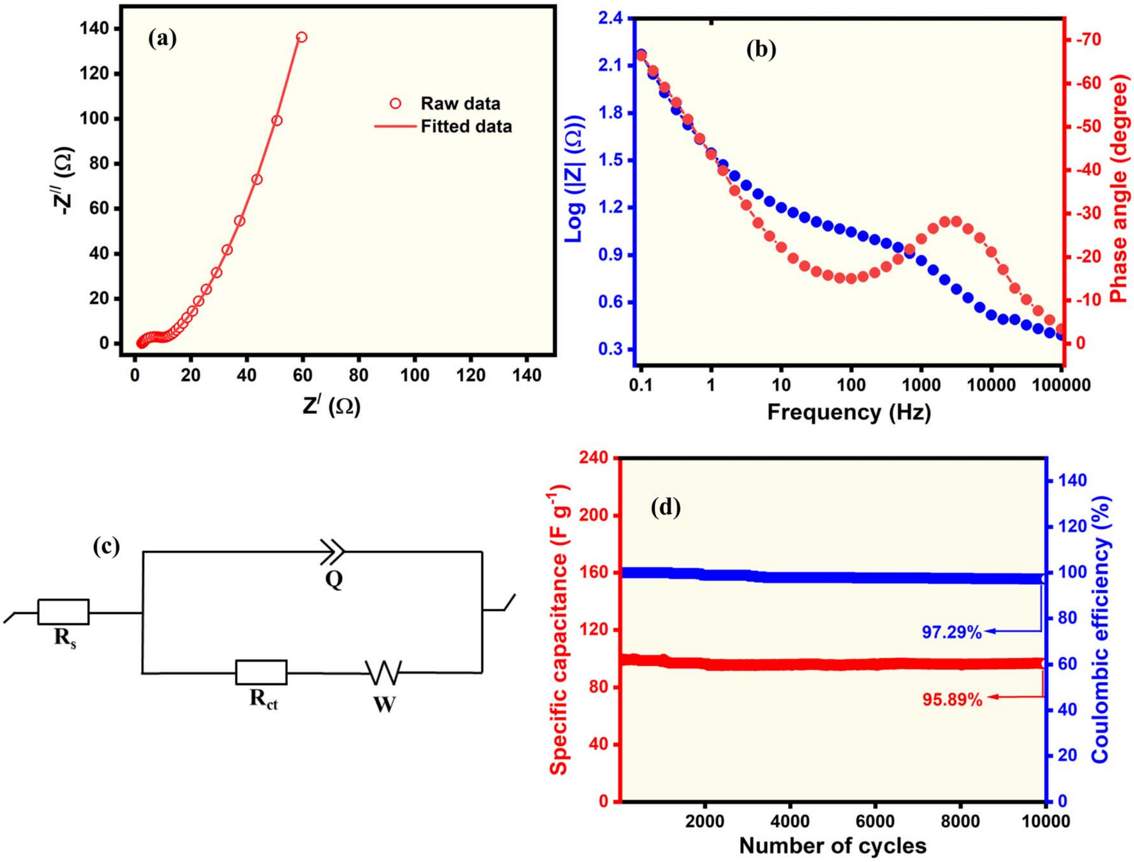

Fig. 7 (a) Nyquist plot, (b) Bode plot of EIS spectra of the device in R-mgpe, (c) equivalent circuit used for fitting the EIS spectra. (d) Cycling stability and coulombic efficiency of the device in R-mgpe recorded at the current density of 7 A g^{-1}.

to 100 mV s^{-1}. The nearly rectangular shape of the CV curves, coupled with the appearance of subtle redox humps, reveals a combination of electric double-layer capacitance (EDLC) and pseudocapacitive behaviour.[17,63] The pseudocapacitive contribution arises from the reversible redox transitions of I^-/I_3^- in the electrolyte. Furthermore, the good retention of CV shape at higher scan rates suggests efficient ion diffusion and charge propagation within the P-Mg-CN electrode, which is attributed to its mesoporous architecture and the improved conductivity induced by the polymer moieties.[13,64] Additionally, the device maintains a stable operating potential window of 1.4 V, demonstrating the excellent electrochemical stability of R-mgpe. On the other hand, the area under the CV curve of the device fabricated with undoped Mg-CN is lower than that of the P-Mg-CN device at all scan rates (Fig. S2a), suggesting that the phosphorus dopant contributes to the overall capacitance. The enhancement in capacitance for the device is attributed to the synergistic electronic and ionic effects. The phosphorus doping introduces electron-rich P–N and P–C sites, which enhance conductivity and create surface defects that serve as active sites for redox reactions. On the other hand, the presence of I^-/I_3^- couple in the electrolyte is expected to act as an electron shuttle, enabling fast charge transfer between electrodes and supplementing electric-double-layer storage with faradaic processes.[17,20] Fig. 6b and S2b show the GCD of the P-Mg-CN and undoped Mg-CN-based device recorded at various current densities. It can be inferred that the GCD curves exhibit nearly symmetric triangular shapes with minor nonlinearity, further confirming the contributions of EDLC and pseudocapacitance in both materials. Besides, it was found that the discharge time of the device decreases with increasing current density, which is consistent with reduced ion diffusion time at higher current rates. The device fabricated with P-Mg-CN electrodes delivers a specific capacitance of 142 F g^{-1} at a current density of 2 A g^{-1}, which is almost twice that of undoped Mg-CN (71.4 F g^{-1}). The variation in specific capacitance with current density is shown in Fig. 6c. The capacitance gradually decreases with increasing current density, retaining approximately 53.36% of its initial value at 10 A g^{-1}, indicating decent rate capability. Fig. 6d presents the Ragone plot of the device, which reveals that the device delivers an energy density of 38.66 Wh kg^{-1} at a power density of 2.8 kW kg^{-1}, and maintains 20.83 Wh kg^{-1} even at 12.61 kW kg^{-1}. It is worth mentioning that the energy density obtained in the present study surpasses the values reported in the literature (Table 1).

The electrochemical impedance spectroscopy (EIS) is utilised to further understand the solution resistance (R_s) and charge transfer resistance (R_{ct}) of the device. The Nyquist spectrum (Fig. 7a) is fitted using an equivalent-circuit model (Fig. 7c) comprising the solution resistance (R_s), charge-transfer resistance (R_{ct}), constant circuit element (CPE) to account for the non-ideal double-layer response of the porous P-Mg-CN, Warburg element (W) to account for ion diffusion and C, which accounts for an outer interface/geometric capacitance.[63,64] The obtained fitting parameters yielded a chi-square (χ^2) value of 0.0133. The equivalent circuit used for fitting the spectrum is shown in Fig. 7c. The small R_{ct} value of 7.032 indicates facile charge transfer at the electrode/electrolyte interface. The steep line in the low-frequency region suggests that the surface-controlled process is the predominant charge storage mechanism.[65] The Bode plot (Fig. 7b) shows a phase angle approaching −70°, which further confirms near-ideal capacitive behaviour. The characteristic frequency at −45° phase angle is used to calculate the relaxation time constant (τ) of the device.[66] Although a τ of 1.106 seconds obtained in the present study is lower than the values reported for redox additive systems, indicating a fast charge/discharge response, it is comparably higher than the value obtained for carbon-based materials in aqueous electrolyte.[67–69] The cycling stability of the device is evaluated by recording GCD cycles at a current density of 7 A g^{-1} over 10 000 cycles.

As shown in Fig. 7d, the symmetric device exhibits excellent cycling stability and retains 95.89% of its initial capacitance after 10 000 GCD cycles. This excellent durability is attributed to the stable framework of P-Mg-CN, which effectively resists volume and structural changes during repeated cycling.[40,70] As seen in Fig. 7d, the device demonstrates an appreciable coulombic efficiency (97.29%), which suggests good reversibility of the KI couple. It is well established that the decrease in the specific capacitance of a supercapacitor when subjected to long-term charge/discharge is mainly caused by (i) an increase in the value of R_s and/or R_{ct} of the device, (ii) a change in the structural/morphology of the electrode materials and (iii) dissolution of the electroactive material into the electrolyte.[7,69,71] As shown in Fig. S3a, both R_s and R_{ct} increase from 1.80 and 7.032 to 4.85 and 90.40 Ω, respectively, before and after 10 000 cycles, an indication of an increase in the overall internal resistance of the device. Additionally, the FTIR spectra presented in Fig. S3b suggest that the PVA + KI gel did not undergo any significant chemical changes after the 10 000 charge–discharge cycle. Although minor surface smoothing and partial collapse of smaller flakes are observed in the SEM images of the P-Mg-CN electrode after cycling stability (Fig. S4), it is evident that it retains its overall structural integrity, an indication that the mechanical stresses imposed during continuous cycling do not induce significant structural degradation. Therefore, the 4.11% loss in specific capacitance could be attributed to the increase in R_s and R_{ct}.

Conclusion

In summary, a high-energy density symmetric supercapacitor was successfully fabricated using P-Mg-CN as electrode material and a PVA–H_2SO_4–KI gel as both separator and electrolyte. The incorporation of KI and PVA introduced reversible I^-/I_3^- redox couples, which enhanced the pseudocapacitive contribution and expanded the voltage window to 1.4 V, respectively. The device achieved a specific capacitance of 142 F g^{-1} at a current density of 2 A g^{-1}, an energy density of 38.66 Wh kg^{-1} at 2.8 kW kg^{-1}, and excellent cycling stability with 95.89% retention over 10 000 cycles. The superior performance is attributed to the synergistic effects of phosphorus-induced conductivity improvement, mesoporous architecture enabling rapid ion diffusion, and redox-mediated electrolyte providing additional faradaic charge storage. This study demonstrates that utilization of R-mgpe represents an effective approach to overcome the inherent energy density limitation of supercapacitors.

Author contributions

Mustapha Balarabe Idris: conceptualization, data curation, formal analysis, investigation, validation, writing and editing. Bhekie B. Mamba: editing, funding acquisition, project administration, Fuku Xolile: editing, funding acquisition, project administration, resources, supervision, visualization, writing – review & editing.

Conflicts of interest

The authors declare that they have no known competing financial interests or personal relationships that could have appeared to influence the work reported in this paper.

Data availability

Data will be made available on request.

Supplementary information (SI) is available. See DOI: https://doi.org/10.1039/d5ra07907a.

Acknowledgements

The authors would like to express their gratitude to the University of South Africa, the Institute for Nanotechnology and Water Sustainability (iNanoWS), College of Science, Engineering, and Technology for funding and research facilities. During the preparation of this work, the author(s) used Grammarly software for spelling, grammar, and punctuation checks. After using this tool, the author(s) reviewed and edited the content as needed and take(s) full responsibility for the content of the published article.

References

1 M. B. Idris, Z. Musa Mohammed, S. Nuhu, H. Aliyu, H. Abba, B. B. Mamba, D. Sappani and F. Xolile, *ACS Omega*, 2025, **10**, 18184–18212.
2 M. B. Idris, S. Nuhu, Z. M. Mohammed, H. Aliyu, H. Abba, F. Xolile and S. Devaraj, *J. Energy Storage*, 2024, **93**, 112322.
3 M. Ntozonke, M. B. Idris, K. E. Sekhosana, M. A. Kebede and X. Fuku, *ChemistrySelect*, 2025, **10**, e05612.
4 H. Niu, N. Zhang, Y. Lu, Z. Zhang, M. Li, J. Liu, W. Song, Y. Zhao and Z. Miao, *J. Energy Storage*, 2024, **88**, 111666.
5 C. Zhang, J. Yan and F. You, *Adv. Appl. Energy*, 2023, **9**, 100116.

6 T. Ramachandran, H. Butt, L. Zheng and M. Rezeq, *J. Energy Storage*, 2024, **99**, 113425.
7 P. V. Vardhan, M. B. Idris, H. Y. Liu, S. R. Sivakkumar, P. Balaya and S. Devaraj, *J. Electrochem. Soc.*, 2018, **165**, A1865–A1873.
8 V. V. Palem, M. B. Idris, T. Subramaniam and D. Sappani, *ChemistrySelect*, 2020, **5**, 5316–5322.
9 H. R. Khan and A. L. Ahmad, *J. Ind. Eng. Chem.*, 2025, **141**, 46–66.
10 A. Patra, M. Shaikh, S. Ghosh, D. J. Late and C. S. Rout, *Sustain. Energy Fuels*, 2022, **6**, 2941–2954.
11 M. B. Idris, B. B. Mamba and F. Xolile, *Diam. Relat. Mater.*, 2025, **160**, 113052.
12 K. W. Nam, C. W. Lee, X. Q. Yang, B. W. Cho, W. S. Yoon and K. B. Kim, *J. Power Sources*, 2009, **188**, 323–331.
13 K. Sun, F. Ran, G. Zhao, Y. Zhu, Y. Zheng, M. Ma, X. Zheng, G. Ma and Z. Lei, *RSC Adv.*, 2016, **6**, 55225–55232.
14 A. D. Shuaibu, S. S. Shah, A. S. Alzahrani and M. A. Aziz, *J. Energy Storage*, 2025, **107**, 114851.
15 A. Patra, P. Mane, S. R. Polaki, B. Chakraborty and C. S. Rout, *J. Energy Storage*, 2022, **54**, 105355.
16 G. Ma, E. Feng, K. Sun, H. Peng, J. Li and Z. Lei, *Electrochim. Acta*, 2014, **135**, 461–466.
17 N. Ahmad, A. Rinaldi, M. Setti, M. Sidoli, S. Scaravonati, V. Vezzoni, G. Magnani, M. Riccò, C. Milanese and M.-M. Titirici, *ACS Appl. Energy Mater.*, 2025, **8**(13), 9391–9406.
18 J. Yang, M. Wang, T. Chen, X. Yu, G. Qin, X. Fang, X. Su and Q. Chen, *Sci. China Mater.*, 2023, **66**, 1779–1792.
19 B. Jinisha, K. Anilkumar, M. Manoj, C. M. Ashraf, V. Pradeep and S. Jayalekshmi, *J. Solid State Electrochem.*, 2019, **23**, 3343–3353.
20 S.-E. Hyeon, J. Y. Seo, J. W. Bae, W.-J. Kim and C.-H. Chung, *Electrochim. Acta*, 2019, **319**, 672–681.
21 Z. Xun, Y. Liu, J. Gu, L. Liu and P. Huo, *J. Electrochem. Soc.*, 2019, **166**, A2300.
22 A. Thomas, A. Fischer, F. Goettmann, M. Antonietti, J.-O. Müller, R. Schlögl and J. M. Carlsson, *J. Mater. Chem.*, 2008, **18**, 4893–4908.
23 A. Wang, C. Wang, L. Fu, W. Wong-Ng and Y. Lan, *Nano-Micro Lett.*, 2017, **9**, 47.
24 L. Kong, P. Song, F. Ma and M. Sun, *Mater. Today Energy*, 2020, **17**, 100488.
25 S. A. Thomas, M. R. Pallavolu, M. E. Khan and J. Cherusseri, *J. Energy Storage*, 2023, **68**, 107673.
26 Y. Tong, J. Xia, Y. Hu, Y. He, G. He and H. Chen, *Chem. Commun.*, 2025, **61**, 1509–1532.
27 K. S. Lakhi, D.-H. Park, K. Al-Bahily, W. Cha, B. Viswanathan, J.-H. Choy and A. Vinu, *Chem. Soc. Rev.*, 2017, **46**, 72–101.
28 H. S. Gujral, G. Singh, J. H. Yang, C. I. Sathish, J. B. Yi, A. Karakoti, M. Fawaz, K. Ramadass, A. H. Al-Muhtaseb, X. J. Yu, M. B. H. Breese and A. Vinu, *Carbon*, 2022, **195**, 9–18.
29 W. Cha, I. Y. Kim, J. M. Lee, S. Kim, K. Ramadass, K. Gopalakrishnan, S. Premkumar, S. Umapathy and A. Vinu, *ACS Appl. Mater. Interfaces*, 2019, **11**, 27192–27199.
30 M. B. Idris, G. Sakthivel and S. Devaraj, *Mater. Today Energy*, 2018, **10**, 325–335.
31 M. B. Idris and S. Devaraj, *J. Energy Storage*, 2019, **26**, 101032.
32 D. Adekoya, X. Gu, M. Rudge, W. Wen, C. Lai, M. Hankel and S. Zhang, *Adv. Funct. Mater.*, 2018, **28**, 1803972.
33 B. Antil, L. Kumar, M. R. Das and S. Deka, *J. Energy Storage*, 2022, **52**, 104731.
34 S. Zhang, Y. Huang, J. Wang, X. Han, C. Chen and X. Sun, *Appl. Surf. Sci.*, 2022, **599**, 154015.
35 P. Chaluvachar, G. Mahesha, V. G. Nair, D. K. Pai and Y. Sudhakar, *Electrochim. Acta*, 2025, **513**, 145605.
36 S. Khan, M. A. Qaiser, W. A. Qureshi, Y. Xu, J. Li, H. Li, L. Sun, S. N.-Z. Haider, B. Zhu and L. Wang, *ACS Appl. Mater. Interfaces*, 2025, **17**, 6249–6259.
37 H. Zhang, W. Tian, X. Duan, H. Sun, Y. Shen, G. Shao and S. Wang, *Nanoscale*, 2020, **12**, 6937–6952.
38 H. Jiang, Y. Li, D. Wang, X. Hong and B. Liang, *Curr. Org. Chem.*, 2020, **24**, 673–693.
39 J. Li, Y. Qi, Y. Mei, S. Ma, Q. Li, B. Xin, T. Yao and J. Wu, *J. Colloid Interface Sci.*, 2020, **566**, 495–504.
40 M. B. Idris, G. H. Sai, D. Hemalatha, G. Sakthivel and S. Devaraj, *J. Electrochem. Soc.*, 2019, **166**, A2409–A2418.
41 A. Kumar, B. N. Mahanty, A. Rawat, R. Muhammad, R. K. Panigrahi, D. Pradhan and P. Mohanty, *Energy Fuels*, 2023, **37**, 6810–6823.
42 R. Meng, S. Tang, B. Xia and X. Chen, *ChemistrySelect*, 2020, **5**, 13862–13867.
43 X. B. Hu, Y. Hu, Q. Zhang, Y. Yu and Y. Q. Wang, *Mater. Test.*, 2020, **62**, 378–382.
44 S. Subburaj, S. Thomas, M. Kavipriyah and B. Subramanian, *Inorg. Chem. Commun.*, 2024, **170**, 113266.
45 M. Qasim, C. Zhang, A. A. Rizvi, F. A. Qaraah, W. Ahmad and Z. Huihui, *Int. J. Hydrogen Energy*, 2025, **173**, 151319.
46 A. Pathak, K. Ahmad, R. A. Khan and T. Oh, *Top. Catal.*, 2025, **68**, 242–251.
47 S. Sunasee, K. H. Leong, K. T. Wong, G. Lee, S. Pichiah, I. Nah, B.-H. Jeon, Y. Yoon and M. Jang, *Environ. Sci. Pollut. Res.*, 2019, **26**, 1082–1093.
48 P. Mary Rajaitha, K. Shamsa, C. Murugan, K. Bhojanaa, S. Ravichandran and K. Jothivenkatachalam, *SN Appl. Sci.*, 2020, **2**, 52.
49 M. B. Idris, T. Subramaniam and D. Sappani, *Diam. Relat. Mater.*, 2022, **129**, 109359.
50 M. Anbia and M. Haqshenas, *Int. J. Sci. Environ. Technol.*, 2015, **12**, 2649–2664.
51 G. D'Altri, L. Yeasmin, V. Di Matteo, S. Scurti, A. Giovagnoli, M. F. Di Filippo, I. Gualandi, M. C. Cassani, D. Caretti, S. Panzavolta, E. Scavetta, M. Rea and B. Ballarin, *ACS Omega*, 2024, **9**, 6391–6402.
52 M. Mohammed, A. Ismail and G. Salem, *Egypt. J. Solid.*, 2017, **40**, 79–94.
53 Z. Yang, J. Tang, H. Zhang, X. Peng, Y. Liu, J. Liu and Q. Guo, *J. Power Sources*, 2025, **652**, 237547.
54 A. Patra and C. S. Rout, *Energy Storage*, 2023, **5**, e411.
55 Y. Liu, B. Cheng, X. Xie, J. Chen, L. Wan, C. Du, Y. Zhang and M. Xie, *Fuel*, 2025, **381**, 133607.
56 G. Rutavi, D. J. Tarimo, V. M. Maphiri, V. N. Kitenge and N. Manyala, *J. Energy Storage*, 2023, **58**, 106442.

57 H. Yu, J. Wu, J. Lin, L. Fan, M. Huang, Y. Lin, Y. Li, F. Yu and Z. Qiu, *ChemPhysChem*, 2013, **14**, 394–399.

58 A. J. Bard, L. R. Faulkner and H. S. White, *Electrochemical Methods: Fundamentals and Applications*, John Wiley & Sons, 2022.

59 H. Fitzek, M. Sterrer, D. Knez, H. Schranger, A. Sarapulova, S. Dsoke, H. Schroettner, G. Kothleitner, B. Gollas and Q. Abbas, *Nanomaterials*, 2023, **13**, 1545.

60 H. Schranger, S. Khosravi, H. Fitzek and Q. Abbas, *ChemElectroChem*, 2021, **8**, 3155–3160.

61 L. D. Larasati, Z. Supiyeva, M. T. Islam and Q. Abbas, *Materials*, 2024, **17**, 3407.

62 L. Zhang, T. Wang, T.-N. Gao, H. Xiong, R. Zhang, Z. Liu, S. Song, S. Dai and Z.-A. Qiao, *CCS Chem.*, 2021, **3**, 870–881.

63 P. Bharathidasan, M. B. Idris, D.-W. Kim, S. Sivakkumar and S. Devaraj, *FlatChem*, 2019, **15**, 100108.

64 S. Alipoori, S. Mazinani, S. H. Aboutalebi and F. Sharif, *J. Energy Storage*, 2020, **27**, 101072.

65 K. Panchal, K. Bhakar, K. S. Sharma, D. Kumar and S. Prasad, *Appl. Spectrosc. Rev.*, 2025, **60**, 30–55.

66 L. E. Helseth, *J. Energy Storage*, 2021, **34**, 102199.

67 L. E. Helseth, *J. Energy Storage*, 2019, **25**, 100912.

68 D. Mu, H. Lin, X. Jiang, Z. Wang, W. Wang and H. Zhang, *Small*, 2025, **21**, 2411996.

69 A. G. Olabi, Q. Abbas, M. A. Abdelkareem, A. H. Alami, M. Mirzaeian and E. T. Sayed, *Batteries*, 2022, **9**, 19.

70 A. Patra, P. Mane, K. Pramoda, S. Hegde, B. Chakraborty and C. S. Rout, *J. Energy Storage*, 2023, **68**, 107825.

71 P. V. Vardhan, M. B. Idris, V. Ramanathan and S. Devaraj, *ChemistrySelect*, 2018, **3**, 6775–6778.

72 A. Dahiru Shuaibu, A. Saeed Alzahrani and M. A. Aziz, *Asian J. Org. Chem.*, 2023, **12**, e202300050.

73 Y. Yang, D. Zhang, Y. Liu, L. Shen, T. Zhu, X. Xu, J. Zheng and X. Gong, *ACS Appl. Mater. Interfaces*, 2021, **13**, 34168–34177.

74 S. A. Sawant, M. R. Waikar, G. R. Chodankar, S. R. Gurav, A. V. Patil, R. S. Vhatkar and R. G. Sonkawade, *J. Energy Storage*, 2024, **76**, 109739.

75 Q.-M. Tu, L.-Q. Fan, F. Pan, J.-L. Huang, Y. Gu, J.-M. Lin, M.-L. Huang, Y.-F. Huang and J.-H. Wu, *Electrochim. Acta*, 2018, **268**, 562–568.